Chapter 18

Direct and Hybrid Aeroacoustic Simulations Around a Rectangular Cylinder

Hiroshi Yokoyama and Akiyoshi Iida

Additional information is available at the end of the chapter

http://dx.doi.org/10.5772/intechopen.70810

Abstract

Aeroacoustic simulations are divided into hybrid and direct simulations. In this chapter, the effects of freestream Mach number on flow and acoustic fields around a two-dimensional square cylinder in a uniform flow are focused on using direct and hybrid simulations of flow and acoustic fields are performed. These results indicate the effectiveness and limit of the hybrid simulations. The Mach number M is varied from 0.2 to 0.6. The propagation angle of the acoustic waves for a high Mach number such as $M = 0.6$ greatly differs from that predicted by modified Curle's equation, which assumes the scattered sound to be dominant and takes the Doppler effects into consideration. This is because the acoustic field is affected by the direct sound, which is generated by quadrupoles in the original Curle's equation. To clarify the effects of the direct sound on the acoustic field, the scattered and direct sounds are decomposed. The results show that the direct sound is too intense to neglect for $M \geq 0.4$. Moreover, acoustic simulations are performed using the Lighthill's acoustic sources.

Keywords: aeroacoustics, aeolian tone, direct simulation, acoustic analogy, Lighthill's equation

1. Introduction

The sound generated by a cylinder in a uniform flow is known as the aeolian tone. This sound is often radiated from flows around a cylinder. Strouhal [1] found that the frequency of the tone is identical to the vortex shedding frequency. Lighthill [2] derived the nonhomogeneous wave equation as shown in Eqs. (1) and (2) from the compressive Navier-Stokes equations.

$$\frac{\partial^2}{\partial t^2}\rho - a_0^2 \frac{\partial^2}{\partial x_i \partial x_j}\rho = \frac{\partial^2 T_{ij}}{\partial x_i \partial x_j}, \tag{1}$$

where ρ is the density, a_0 is the freestream sound speed, and the tensor $\boldsymbol{T}_{ij}$ is defined by:

$$T_{ij} = \rho v_i v_j + \delta_{ij}\left((p - p_0) - a_0^2(\rho - \rho_0)\right) - \tau_{ij}, \tag{2}$$

where v_i is velocity, p is pressure, the tensor $\boldsymbol{\tau}$ is the viscous stress tensor, and $\partial^2 T_{ij}/\partial x_i \partial x_j$ is referred to as Lighthill's acoustic source. The first, second, and third terms of the Lighthill's acoustic source are related to the momentum, entropy, and viscosity, respectively. For aerodynamic sound around a body in a fluid stream of a low Mach number, Curle [3] has shown through analytical solution of Lighthill's equation [2] that the surface pressure fluctuations around the body lead to a dipole sound field. Investigations such as those by Gerrard [4] and Phillips [5] have experimentally confirmed that the acoustic field around a circular cylinder has directivity normal to the fluid stream and is closely related to the fluctuations of the lift force.

Recently, many investigations using numerical simulations have been performed, for instance, Inoue and Hatakeyama [6], Gloerfelt et al. [7], and Liow et al. [8]. Inoue and Hatakeyama [6] modified the Curle's solution considering the Doppler effects and showed that the acoustic fields predicted by the proposed equation agree well with those predicted by their direct simulations for a low freestream Mach number $M \leq 0.3$. Gloerfelt et al. [7] performed incompressible flow computations and acoustic computations on the basis of Lighthill's acoustic analogy [2] for the flow around a circular cylinder. The role of the acoustic scattering on the cylinder in the mechanism of the sound generation was investigated for $M = 0.12$ and the Reynolds number based on the diameter $\mathrm{Re_d} \approx 1.1 \times 10^5$. Here, the entropy (second) and viscous (third) terms in Lighthill's acoustic source Eq. (2) were neglected. This is reasonable for the flow of such a high Reynolds number and a low Mach number [9]. Liow et al. [8] also performed the incompressible flow simulations and acoustic simulations for a flow around an elongated rectangular cylinder with $M \leq 0.2$. The acoustic computations are based on the Powell's theory [10], where the acoustic sources approximately correspond to the momentum (the first term) of Lighthill's acoustic source. The effects of the drag force on the acoustic field were clarified.

Despite many investigations into the aeolian sound around a cylinder, little attention has been given to flows around a cylinder with a high Mach number $M > 0.3$. For such a high Mach number, the effects of the Mach number on the flow and acoustic fields around a cylinder have not been clarified. Also, it is currently unknown whether the contribution of the second and third terms in Lighthill's acoustic source to the acoustic field can be neglected for such a high Mach number. In high-speed jets such as $M = 0.9$–2.0, it has been clarified that the second term needs to be taken into consideration [11].

In the present chapter, aerodynamic sound radiated from a two-dimensional square cylinder in a freestream is investigated. The flow field around a square cylinder has been investigated by many researchers [12–14]. However, little is known about the acoustic field. The hybrid and direct simulations of flow and acoustic fields are introduced. The freestream Mach number on the flow and acoustic fields are focused on. The Mach number is varied from 0.2 to 0.6. Moreover, the contributions of each term of Lighthill's acoustic source to the acoustic field are focused on. To do this, the acoustic simulations are also performed using the Lighthill's acoustic sources computed by the direct simulations. This method for predicting the acoustic field using the acoustic simulation is referred to as the hybrid simulation in this chapter.

http://dx.doi.org/10.5772/intechopen.70810

2. Numerical methods

2.1. Flow configurations

The flow around a two-dimensional square cylinder, as shown in **Figure 1**, is investigated. To clarify the effects of the freestream Mach number on flow and acoustic fields, the computations are performed for M = 0.2, 0.3, 0.4, 0.5, and 0.6. The Reynolds number based on the freestream velocity and the side length of the cylinder is set to 150, where the three-dimensional instability does not occur [13]. Here, the two-dimensional phenomena related to the vortex shedding from the cylinder are focused on.

The fluid was assumed to be standard air, where Sutherland's formula can be applied for the viscosity coefficient. The specific heat C was assumed to be 1004 J kg^{-1} K^{-1} and that the Prandtl number Pr was 0.72.

2.2. Direct simulation

2.2.1. Governing equations and finite difference formulation

Both flow and acoustic fields are solved by the two-dimensional compressible Navier-Stokes equations in a conservative form, which is written as:

$$\boldsymbol{Q}_t + (\boldsymbol{E} - \boldsymbol{E}_{\mathrm{v}})_x + (\boldsymbol{F} - \boldsymbol{F}_{\mathrm{v}})_y = 0, \tag{3}$$

where $\boldsymbol{Q}$ is the vector of the conservative variables, $\boldsymbol{E}$ and $\boldsymbol{F}$ are the inviscid fluxes, and $\boldsymbol{E}_{\mathbf{v}}$ and $\boldsymbol{F}_{\mathbf{v}}$ are the viscous fluxes. The spatial derivatives and time integration were evaluated by the sixth-order accurate compact finite difference scheme [15] and a third-order accurate Runge-Kutta method. To suppress the numerical instabilities associated with the central differencing in the compact scheme, we use a tenth-order accurate spatial filter shown below:

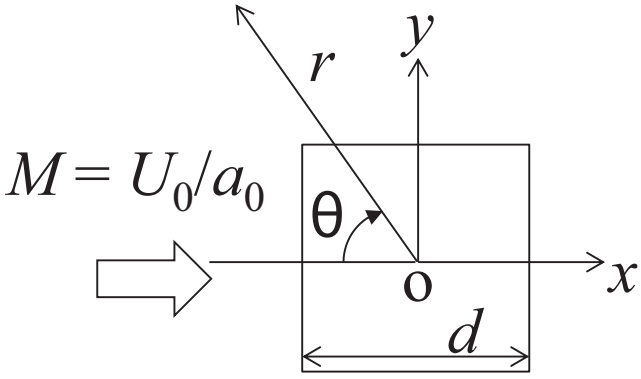

Figure 1. Configurations for flow around a two-dimensional square cylinder.

$$\alpha_f \widehat{\varphi}_{i-1} + \widehat{\varphi}_i + \alpha_f \widehat{\varphi}_{i+1} = \sum_{n=0}^{5} \frac{a_n}{2} (\varphi_{i+n} + \varphi_{i-n}), \tag{4}$$

where φ is a conservative quantity and $\widehat{\varphi}$ is the filtered quantity. The coefficients a_n are the same as the values used by Gaitonde and Visbal [16], and the parameter α_f is 0.47.

2.2.2. Computational grids and boundary conditions

Figure 2 shows the computational domain and boundary conditions. The coordinates originate from the center of the cylinder. Generally, the nonreflecting boundary conditions based on the characteristic wave relations [17–19] are used at the inflow, upper, and outflow boundaries along with a buffer region. The role of the buffer region is similar to that of the "sponge region" of Colonius et al. [20]. At the wall, the nonslip and adiabatic boundary conditions are used.

For all the cases of M = 0.2–0.6, the same grids are used. The computational domain is divided into three regions of different grid spacings as shown in **Figure 2**: a vortex region [$-4.0 \le x/d \le 30.0$, $-4.0 \le y/d \le 4.0$], a sound region [$-70.0 \le x/d < -4.0$, $30.0 < x/d \le 70.0$, $-70.0 \le y/d < -4.0$, $4.0 < y/d \le 70.0$], and a buffer region [$-500.0 \le x/d < -70.0$, $70.0 < x/d \le 500.0$, $-500.0 \le y/d < -70.0$, $70.0 < y/d \le 500.0$].

The spacing in the vortex region is prescribed to be fine enough to analyze the separated shear layer and the vortical structures in the wake of the cylinder. **Figure 3** shows the computational grid near the cylinder. The spacing adjacent to the cylinder surface is $\Delta x_{min}/d$ and $\Delta y_{min}/d$ = 0.0025. With this grid distribution, the number of grid points within the separated shear layer for Re = 150 is 22 in the x, y direction (the thickness of the separated shear layer was estimated by $\delta/d \sim 1/Re^{0.5}$ and 0.08 for Re = 150 like the circular cylinder [6]), and the separated shear layer can be sufficiently captured. In the whole vortex region, $\Delta x/d$ and $\Delta y/d$ are less than 0.2, where the

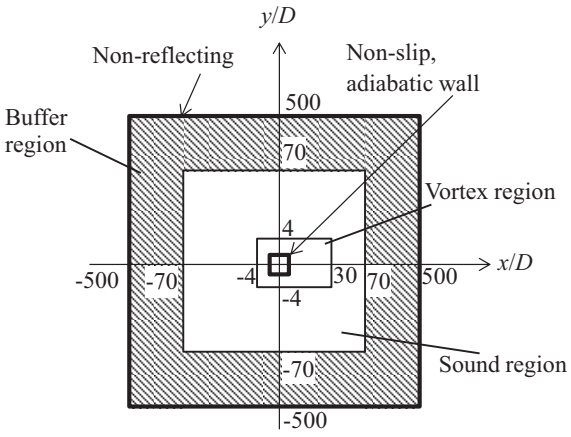

Figure 2. Computational domain and boundary conditions for direct simulations.

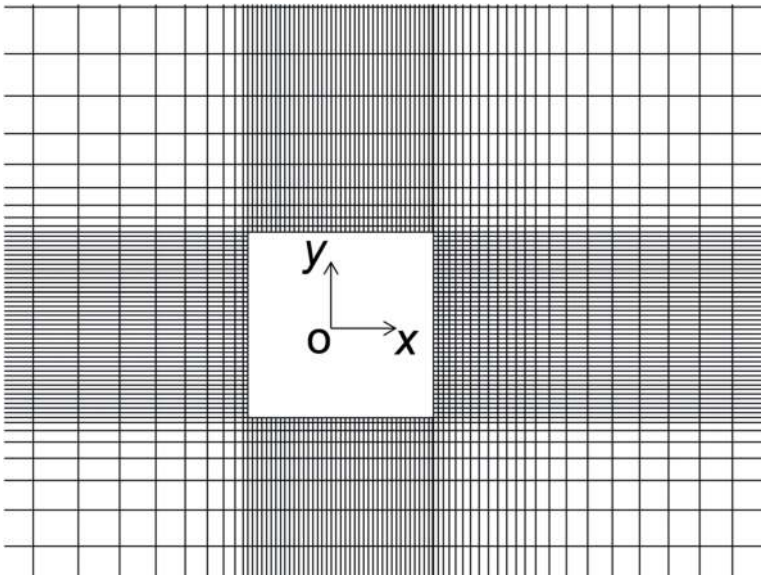

Figure 3. Computational grid near cylinder for direct simulations. Every 10th grid line is shown for clarity.

number of grid points within a shed vortex is about 15 in the x, y direction (the size of the vortex is estimated to be about $3d$ by the spacing of the local maxima of vorticity in the computational results) and the vortices were sufficiently analyzed.

In the sound region, the spacing is prescribed to be larger than that in the vortex region but still fine enough to capture the acoustic waves. The spacings are $\Delta x/d$, $\Delta y/d \leq 0.23$ except for the downstream region of the cylinder. In the downstream region, the largest spacings are $\Delta x/d$ and $\Delta y/d = 0.46$. This is because the acoustic wavelength becomes longer than that in the upstream region due to the Doppler effects. In the whole sound region, more than 20 grid points are used per one acoustic wavelength of the tonal sound at the frequency of the vortex shedding, and the acoustic waves are sufficiently captured.

After many preliminary tests, grid- and domain-size independence has been established for the solutions presented in this chapter.

2.3. Hybrid simulation

2.3.1. Governing equations and discretization formulation

The two-dimensional Lighthill's equation [Eqs. (1) and (2)] is solved based on the wave equation. Here, the open-source software, FrontFlow/blue-ACOUSTICS, was used. Here, the acoustic simulations are performed in a frequency domain using finite-element methods. A component perturbed at the frequency f of quantify g_f can be written as:

$$g_f = \tilde{g}_f(\mathbf{x})e^{i2\pi ft}. \tag{5}$$

Using Eq. (5), Lighthill's equation can be written as:

$$\frac{\partial^2 \tilde{\rho}_f}{\partial x_i \partial x_j} + k^2 \tilde{\rho}_f = -\frac{1}{a_0^2}\frac{\partial^2 \tilde{T}_{ij,f}}{\partial x_i \partial x_j}, \tag{6}$$

where $k = 2\pi f/a_0$ is the wavenumber. The right-hand side of Eq. (6) is computed by the results of the direct simulation in the present chapter. Also, acoustic waves at the frequency of the vortex shedding are focused on. To minimize the spurious errors, the computed acoustic sources are reduced smoothly to zero near the outflow boundary of the acoustic simulation by using the filter. **Figure 4** shows the computational domain for the acoustic simulations and the outer shape of computational domain is circular with the cylinder at its center, and the radius is $100D$. The above-mentioned filter is defined as:

$$\widehat{A} = A \times G(r - r_0), \tag{7}$$

$$A = \partial^2 \frac{\tilde{T}ij,f}{\partial xi \partial xj}, \tag{8}$$

$$G(r_d) = \begin{cases} \frac{1}{2}\left(1 + \cos\frac{r_d}{L}\pi\right) & (80.0 < r \leq 100.0) \\ 1.0 & (r \leq 80.0) \end{cases}, \tag{9}$$

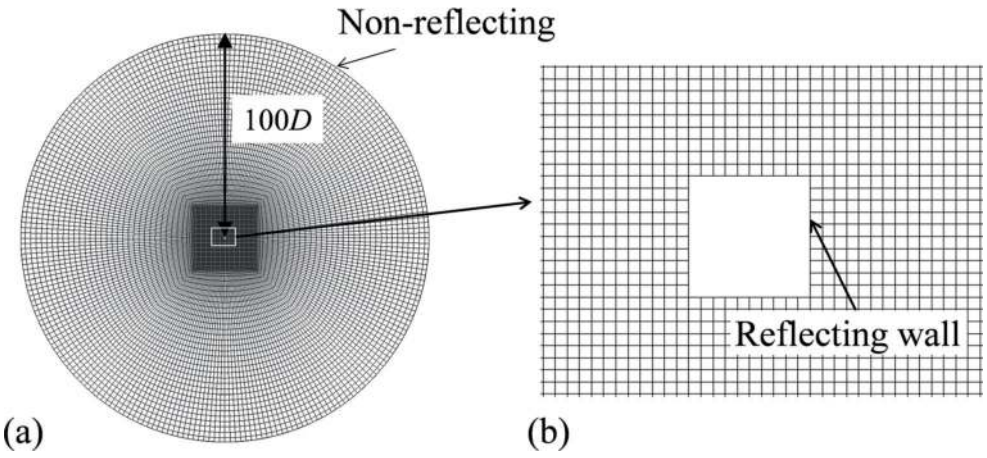

Figure 4. Computational grids and boundary conditions for acoustic simulations. (a) Overall grids (every fifth grid line is shown for clarity) and (b) grids near cylinder (every grid line is shown).

$$r0/d = 80.0, L/d = 20, \tag{10}$$

where r is the distance from the center of the cylinder.

2.3.2. Computational grids and boundary conditions

Figure 4 shows the computational grid for the acoustic simulations. The spacing adjacent to the cylinder surface is $\Delta x_{\min}/d$ and $\Delta y_{\min}/d = 0.1$. In the whole domain, the grid spacing is less than 0.52, and more than 20 grid points are used per acoustic wavelength. The preliminary computations confirmed that the acoustic waves are sufficiently analyzed with these grid resolutions.

The reflecting conditions are adopted on the cylinder wall. On the other boundaries, the nonreflecting boundary conditions are adopted.

3. Validation of computational methods

3.1. Validation of direct simulations

Figure 5 shows the Strouhal number of vortex shedding predicted by the present direct simulations. The Strouhal number St is the frequency nondimensionalized by the freestream velocity U_0 and the side length of the cylinder d. The present results are compared with the results of the past incompressible simulation (St = 0.155) [13] and those of the past experiment (St = 0.162) [14] for the same Reynolds number. The flow condition of the experiment is approximately incompressible. The present Strouhal numbers for all the Mach numbers are slightly lower than those in past results. The present computational results show that the Strouhal number becomes lower as the freestream Mach number becomes higher. This is

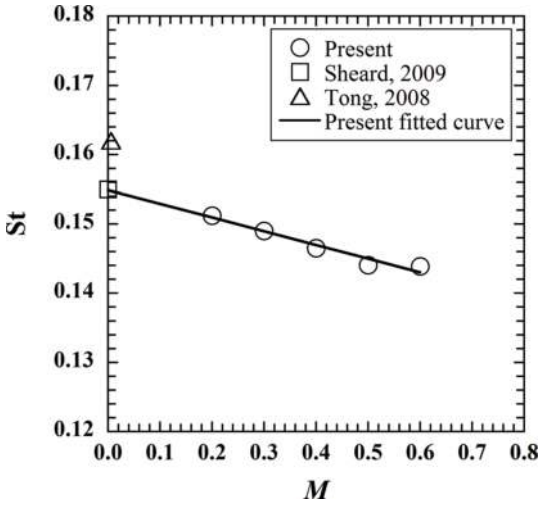

Figure 5. Effects of Mach number on frequency of vortex shedding.

related to the variation of vortices with the variation of the Mach number as discussed in detail in Section 4.1. Also, based on the present results, the extrapolated Strouhal number at $M = 0.0$ is 0.155. This value agrees well with the past computational data [13], although it is not clear why the past experimental value [14] is slightly higher. Consequently, the present direct simulations are confirmed to be validated.

3.2. Validation of hybrid simulation

Figure 6 shows the polar plots of the sound pressure levels at $r/d = 30.0$ predicted by direct and hybrid simulations for $M = 0.4$. The acoustic field by the hybrid simulation is approximately in good agreement with that by the direct simulation. It has been confirmed that the two fields also agree for other Mach numbers such as $M = 0.2$ and 0.6. The above-mentioned methods of hybrid simulation are clarified to be validated.

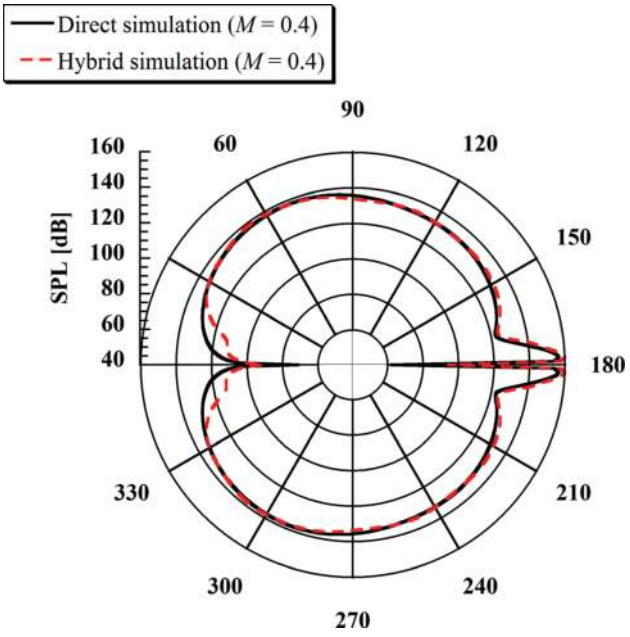

Figure 6. Polar plots of sound pressure levels by direct and hybrid simulations at $r/d = 30.0$ for $M = 0.4$.

4. Results and discussion

4.1. Flow fields

Figure 7 shows the contours of vorticity for $M = 0.2$, 0.4, and 0.6. The periodic vortex shedding was clarified to occur. The effects of the freestream Mach number on the frequency of the vortex shedding are shown in **Figure 5**. As mentioned above, it was found that the Strouhal number becomes lower as the Mach number becomes higher. The Strouhal number for $M = 0.2$

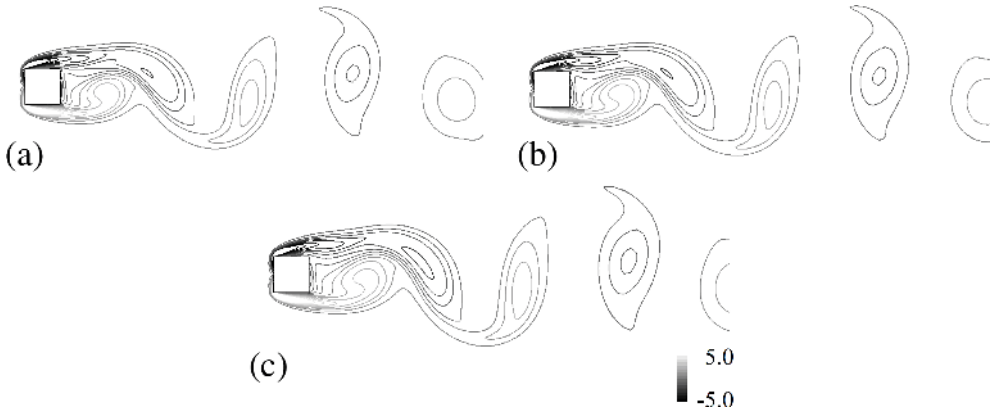

Figure 7. Contours of vorticity $\omega_z/(U_0/d)$. (a) $M = 0.2$, (b) $M = 0.4$, and (c) $M = 0.6$.

is 0.151 and that for $M = 0.6$ is 0.144. Here, to clarify the reason, the Strouhal number becomes lower, and the flow fields are discussed.

Figure 8(a) shows the mean streamwise velocity at $x/D = 1.0$ for $M = 0.2$, 0.4, and 0.6. **Figure 8(b)** shows the half-value width of that profile, d_h, for $M = 0.2$–0.6. The half-value width is shown to increase as the freestream Mach number becomes higher. Also, **Figure 9** shows the mean streamwise Reynolds stress u_{1rms}/U_0. This figure shows that the Reynolds stress becomes larger as the freestream Mach number becomes higher. This means that the velocity fluctuations of the vortices intensify. Due to this intensification, the recovery of the mean streamwise in the wake becomes more rapid and the wake becomes wider as mentioned above. This change is different

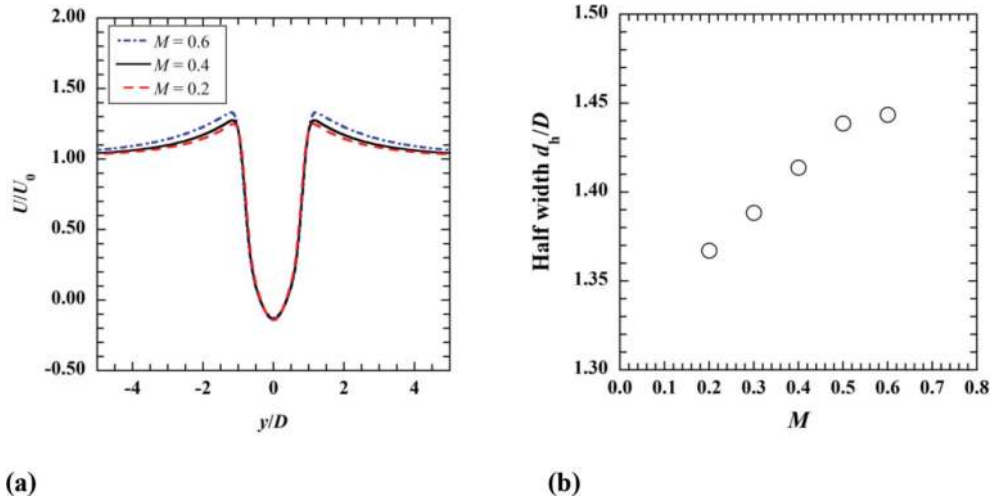

Figure 8. (a) Mean streamwise velocity at $x/D = 1.0$ ($M = 0.2$, 0.4, and 0.6) and (b) half-value width of mean streamwise velocity at $x/D = 1.0$ for $M = 0.2$–0.6.

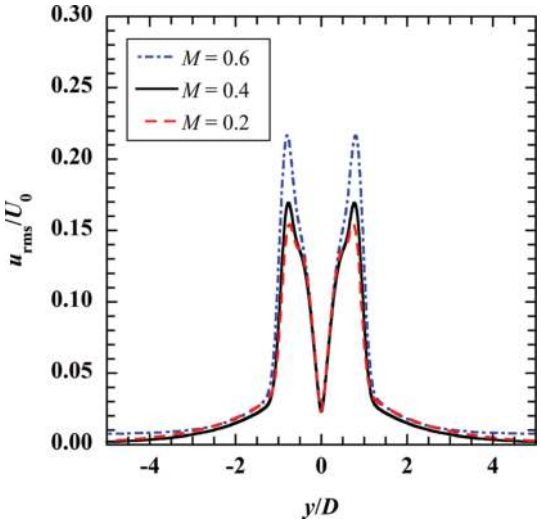

Figure 9. Mean streamwise Reynolds stress $u_{1\mathrm{rms}}/U_0$ (M = 0.2, 0.4, and 0.6).

from that of the vortices in the turbulent mixing layer [21], where the vortices become weaker with compressibility for a higher Mach number.

A possible reason the Reynolds stress becomes larger is that the acoustic feedback like that in the oscillations in cavity flows [22] also exists in the present cylinder flow and the acoustic waves affect the shed vortices. In this case, as the freestream Mach number becomes higher, the acoustic wave intensifies as shown in Section 4.2 and the shed vortex intensifies due to the acoustic feedback.

Roshko [23] showed that the frequency of the vortex shedding around a bluff body is proportional to the wake width. Here, to clarify the relationship between the wake width and the frequency of the vortex shedding, the modified Strouhal number $\mathrm{St_d}$, which is defined by Eq. (11), was computed.

$$\mathrm{St_d} = fd_\mathrm{h}/U_0. \tag{11}$$

Figure 10 shows the effects of the freestream Mach number on the modified Strouhal number $\mathrm{St_d}$. This figure clarifies that the modified Strouhal number is approximately independent of the Mach number. Consequently, it is confirmed that the original Strouhal number decreases because the wake becomes wider. As mentioned above, the intensification of the velocity fluctuations of the vortices widens the wake.

4.2. Acoustic radiation

Figure 11 shows the contours of pressure fluctuations with the time-averaged pressure subtracted for M = 0.4. For the same Mach number, **Figure 12** shows the contours of the second

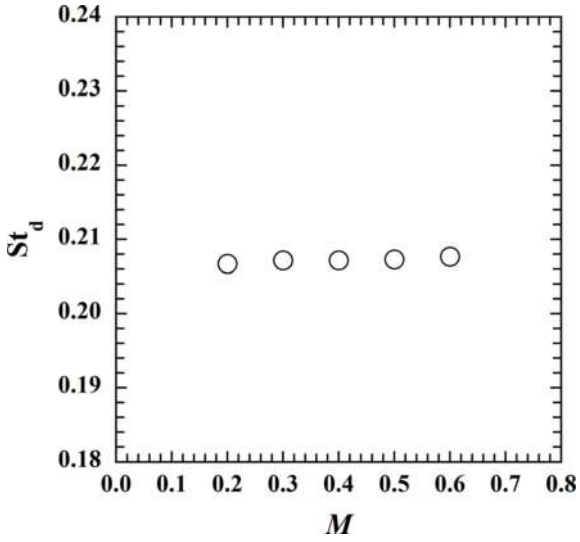

Figure 10. Modified Strouhal number.

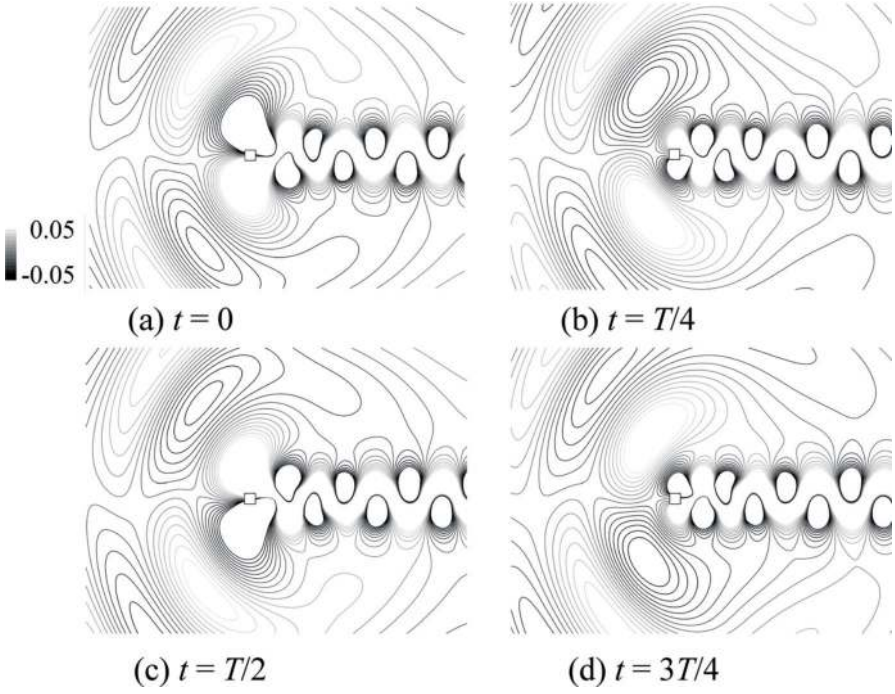

Figure 11. Contours of pressure fluctuations $p'/(\rho_0 a_0{}^2 M^{3.5})$ ($M = 0.4$). (a) $t = 0$, (b) $t/T = 1/4$, (c) $t/T = 1/2$, and (d) $t/T = 3/4$ (T is the period).

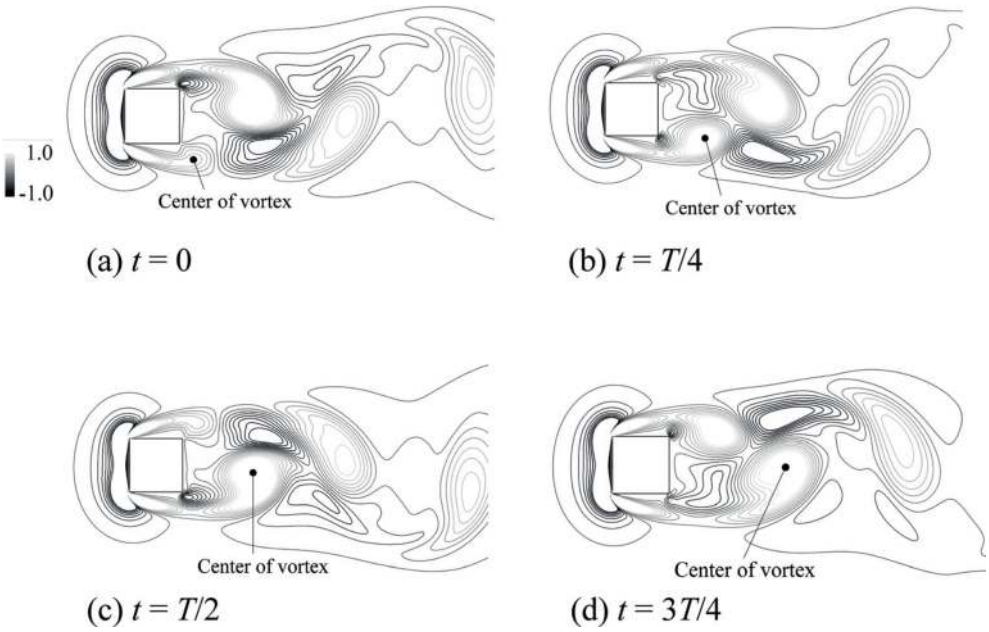

Figure 12. Contours of the second invariant of velocity gradient tensor ($M = 0.4$). (a) $t = 0$, (b) $t/T = 1/4$, (c) $t/T = 1/2$, and (d) $t/T = 3/4$ (T is the period).

invariant of velocity gradient tensor $q = ||\mathbf{\Omega}||^2 - ||\mathbf{S}||^2$ is computed, where $\mathbf{\Omega}$ and $\mathbf{S}$ are, respectively, the asymmetric and symmetric parts of the velocity gradient tensor. Regions with $q > 0$ represent vortex tubes. These figures show that when the vortex is shed from the cylinder, an expansion wave is radiated on that side. For example, the expansion wave is radiated from the lower side of the cylinder in **Figures 11(b)** and **12(b)**. Meanwhile, a compression wave is radiated from the other side. This relationship of the vortex shedding and acoustic radiation is consistent with the computational results of flows around a circular cylinder by Inoue and Hatakeyama [6]. The acoustic radiation mechanism is discussed in detail.

Figure 13 shows the time histories of the pressure and density at the center of a shed vortex, where the positions of the vortex center are estimated by the local maxima of the second invariant and indicated in **Figure 12**. The pressure and density are nondimensionalized by the values at $t = 0$ (the time of $t = 0$ corresponds to **Figures 11(a)** and **12(a)**). Also, the density is raised to the power of the specific ratio γ. This figure shows that the variation of the density is approximately in good agreement with that of pressure. This means that these phenomena are adiabatic. Also, **Figure 13** shows that both the pressure and density become lower as the vortex is developed from $t = 0$ (**Figures 11(a)** and **12(a)**) to $t = T/4$ (**Figures 11(b)** and **12(b)**). This means that the fluid in the vortex expands. As a result, an expansion wave is radiated when the vortex is shed. After the shedding, the density in the vortex becomes higher and recovers to the initial value. At this time, a compression wave is radiated between the expansion waves. This radiation mechanism is independent of the freestream Mach number.

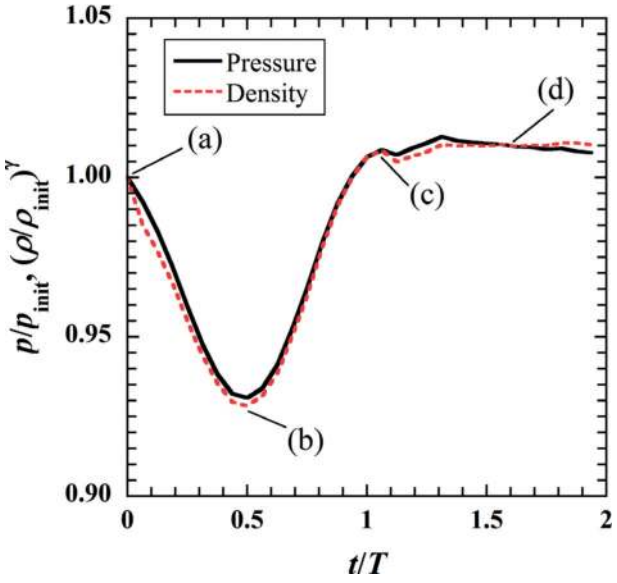

Figure 13. Time histories of pressure and density at the center of the vortex. The letters in this figure correspond to the captions of **Figures 11** and **12**.

4.3. Acoustic fields

4.3.1. Directivity of acoustic wave

Figure 14 shows the contours of the pressure fluctuations and the propagation angle of the peak of the acoustic wave, which is referred to as the propagation angle in the following. The propagation angle is compared with the theoretical angle proposed by Inoue and Hatakeyama [6]. In this theory, the scattered sound in Curle's equation [3] is assumed to be dominant, and the sound speed is assumed to be varied by the Doppler effects as indicated in Eq. (12).

$$a_\theta(\theta) = a_0\left(\sqrt{1 - M^2 \sin^2\theta} - M\cos\theta\right), \tag{12}$$

where θ is an angle as shown in **Figure 1**. For M = 0.2, the propagation angle θ = 75° is approximately in good agreement with the theoretical angle θ = 79°. However, the propagation angle θ = 80° greatly differs from the theoretical angle θ = 62° for M = 0.6. This is because the direct sound in Curle's equation [3] becomes more intense as the freestream Mach number becomes higher. The contributions of direct and scattered sounds to total sound are presented quantitatively in Section 4.3.2.

4.3.2. Decomposition of scattered and direct sounds

The sound predicted by the direct simulation is decomposed into scattered and direct sounds. The direct sound p_{direct} is defined as.

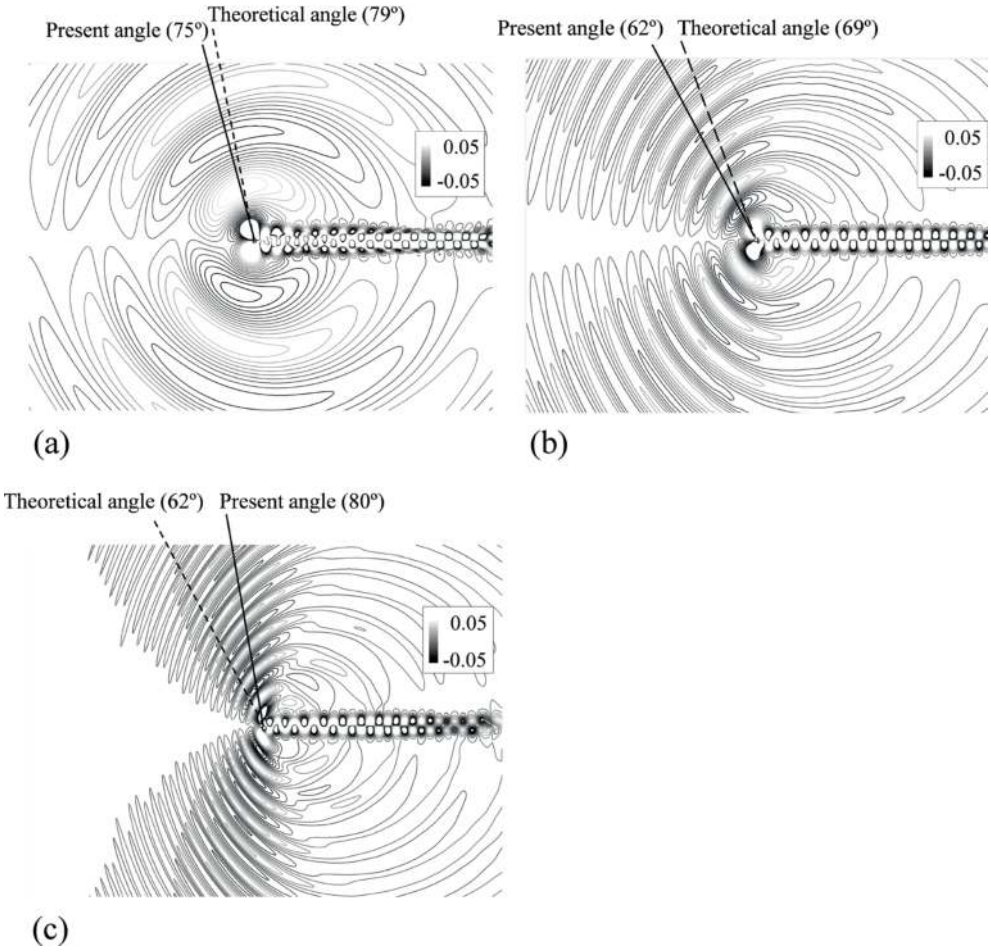

Figure 14. Contours of pressure fluctuations $p'/(\rho_0 a_0{}^2 M^{3.5})$ and propagation angle. Here, (a) $M = 0.2$, (b) $M = 0.4$, and (c) $M = 0.6$.

$$p_{\text{direct}}(t) = p_{\text{total}}(t) - p_{\text{scatter}}(t), \tag{13}$$

where the p_{scatter} is the dipole sound that contains the Doppler effect [6]. Also, the acoustic wavelength is $11.6D$ and so is sufficiently large even for $M = 0.6$ to neglect the difference in the retarded time on the cylinder. The scattered sound p_{scatter} is

$$\begin{aligned} p_{scatter} &= \frac{1}{2^{3/2}\pi a_\theta^{1/2} r^{1/2}} \int_{\tau_0}^{\tau} \frac{F'(\tau')}{\sqrt{\tau - \tau'}} d\tau', \\ F' &= F'_x \cos\theta + F'_y \sin\theta. \end{aligned} \tag{14}$$

where $\tau = t - r/a_0$ and F'_x and F'_y are the time derivatives of the forces exerted on the fluid by the cylinder. Also, the start point of the time integration τ_0 is set to τ −10 T to enlarge the integration interval sufficiently.

Figure 15 shows the polar plots of pressure levels of the total, scattered, and direct sounds at r/D = 30.0 for M = 0.2, 0.4, and 0.6. **Figure 16** shows the effects of the freestream Mach number on each sound pressure levels at r/D = 30.0 in the above-mentioned propagation angle as shown in **Table 1**. For M > 0.3, the sound pressure level of the total sound is proportional to M^7, although that is proportional for M^5 for $M \leq 0.3$. According to the two-dimensional Curle's

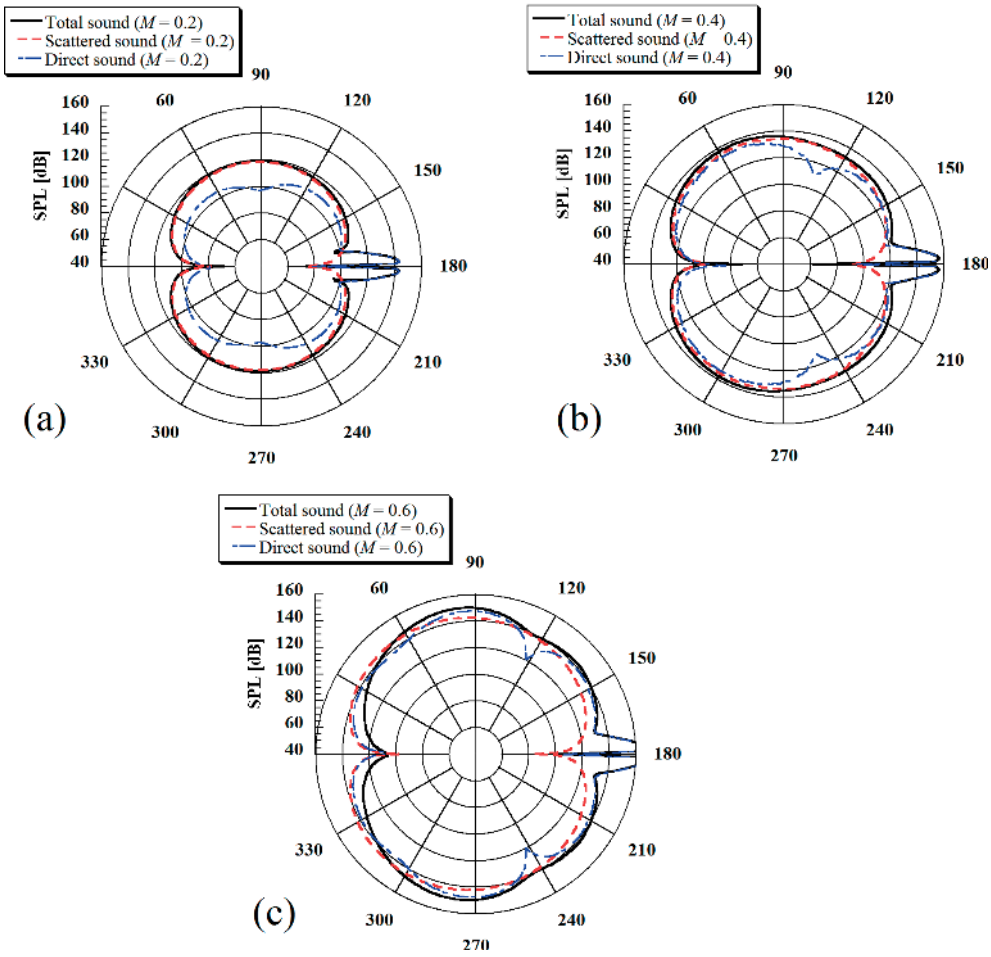

Figure 15. Polar plots of total, scattered, and direct acoustic fields at r/D = 30.0. (a) M = 0.2, (b) M = 0.4, and (C) M = 0.6 [24].

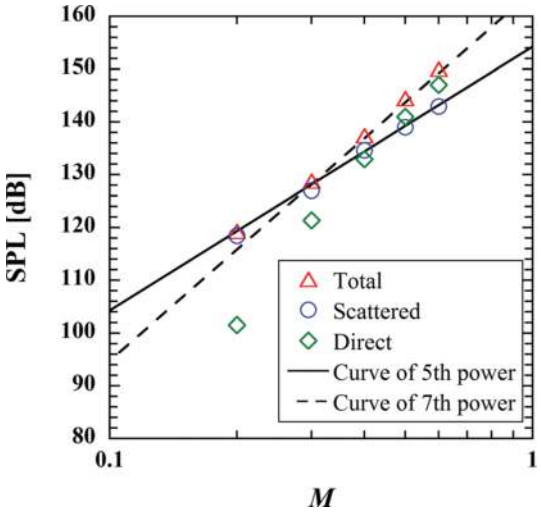

Figure 16. Effects of freestream Mach number on sound pressure levels of total, scattered, and direct sounds at the frequency of the vortex shedding at $r/D = 30.0$ in the direction of acoustic propagation angle [24].

Mach number	0.2	0.3	0.4	0.5	0.6
Present propagation angle	75	64	62	67	80

Table 1. Propagation angle of acoustic waves.

equation introduced by Inoue and Hatakeyama [6], the pressure level of the direct sound is proportional to M^7, whereas that of the scattered sound is proportional to M^5. The present results clarified that sound pressure levels of scattered and direct sounds intersect around $M = 0.4$.

Consequently, it was confirmed that the effects of the direct sound need to be taken into consideration when predicting the sound radiating from a cylinder flow for $M \geq 0.4$. Also, as shown in **Figure 14**, the directivity of the acoustic field for such a high Mach number cannot be predicted by the modified Curle's equation [6], which assumes the scattered sound to be dominant and takes the Doppler effects into consideration. To the authors' knowledge, this is the first time that the effects of the freestream Mach number on the contributions of the scattered and direct sounds have been quantitatively clarified for flows around a cylinder.

4.4. Lighthill's acoustic sources

The right-hand term of Lighthill's equation [Eq. (6)] can be decomposed into three components,

$$\frac{\partial^2 \tilde{T}_{ij}}{\partial x_i \partial x_j} = \frac{\partial^2 \tilde{T}^1_{ij}}{\partial x_i \partial x_j} + \frac{\partial^2 \tilde{T}^2_{ij}}{\partial x_i \partial x_j} + \frac{\partial^2 \tilde{T}^3_{ij}}{\partial x_i \partial x_j}, \tag{15}$$

$$T_{ij}{}^1 = \rho v_i v_j, \quad T_{ij}{}^2 = \delta_{ij}\big((p - p_0) - a_0^2(\rho - \rho_0)\big), \quad T_{ij}{}^3 = -\tau_{ij}. \tag{16}$$

Figure 17 shows the contours of the total Lighthill's acoustic sources $\partial^2 \tilde{T}_{ij}/\partial x_i \partial x_j/\left(\rho_0 U_0^2/D^2\right)$ at the frequency of the vortex shedding in (a), those of the first term $\partial^2 \tilde{T}^1_{ij}/\partial x_i \partial x_j/\left(\rho_0 U_0^2/D^2\right)$ in (b), and those of the second term $\partial^2 \tilde{T}^2_{ij}/\partial x_i \partial x_j/\left(\rho_0 U_0^2/D^2\right)$ in (c) (hereafter referred to as first and second terms, respectively). Here, the third term is negligibly small, so its contour is not presented here. All the contours show that the acoustic sources near the cylinder are more intense than the acoustic sources in the wake far from the cylinder. This is because the acoustic waves are radiated by the vortex shedding from the cylinder as mentioned above. Also, the intensity of the second term, which is usually neglected for the acoustic prediction using Lighthill's acoustic analogy [7, 8], was found to be comparable to that of the first term.

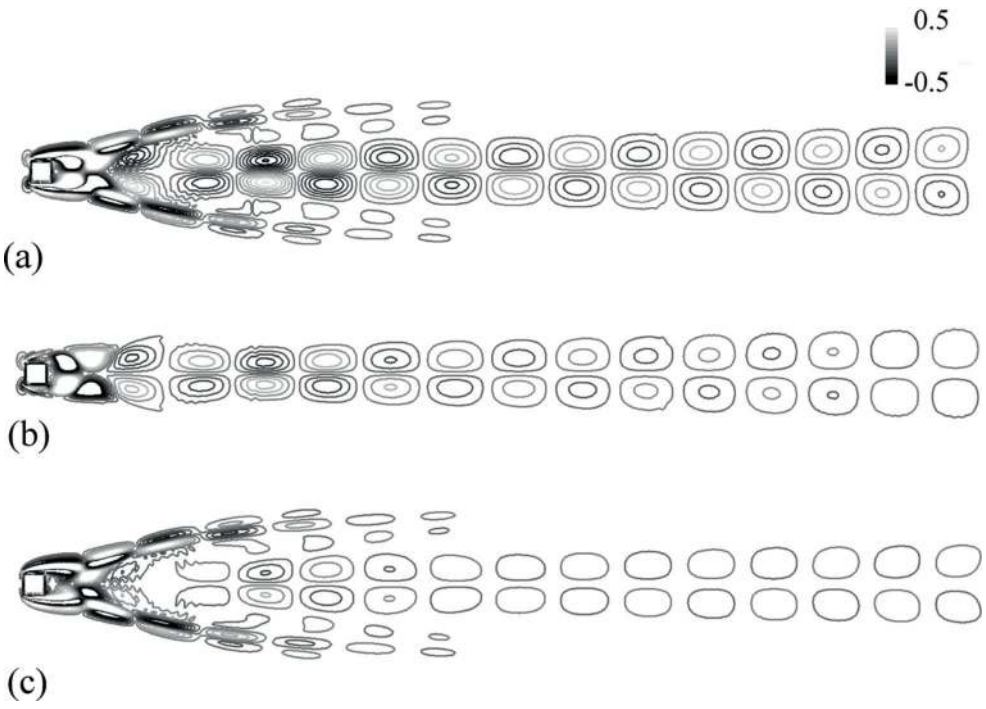

Figure 17. Lighthill's acoustic sources for $M = 0.4$ (real part is shown). (a) All terms $\partial^2 \tilde{T}_{ij}/\partial x_i \partial x_j/\left(\rho_0 U_0^2/D^2\right)$, (b) first term $\partial^2 \tilde{T}^1_{ij}/\partial x_i \partial x_j/\left(\rho_0 U_0^2/D^2\right)$, and (c) second term $\partial^2 \tilde{T}^2_{ij}/\partial x_i \partial x_j/\left(\rho_0 U_0^2/D^2\right)$.

To clarify the contributions of each term to the acoustic field, four hybrid simulations were performed for each Mach number on the basis of total Lighthill's acoustic sources computed by the direct simulation, only the first term, only the second term, and only the third term.

Figure 18 shows the polar plots of the sound pressure level at the frequency of the vortex shedding predicted at $r/D = 30.0$ by the hybrid simulations for $M = 0.4$. It was clarified that the sound pressure levels predicted by the hybrid simulation based on all terms agree well with those based on only the first term. The sound pressure level based on the second term and that on the third term is negligibly weaker than that based on the first term. Meanwhile, the intensity of the second term is in itself comparable to that of the first term as mentioned above. This indicates that the radiation efficiency of the second term is weaker than that of the first term.

Figure 19 shows the predicted sound pressure level at $r/D = 30.0$ in the direction of the above-mentioned acoustic propagation angle. The results clarified that the first term is the dominant acoustic source for all the Mach numbers. The difference between the sound pressure level based on the first term and that based on the second or third term was more than 30 dB for all the Mach numbers. This result shows that the momentum (the first term) of Lighthill's acoustic source is the dominant acoustic source for all the Mach numbers for cylinder flows, while it has

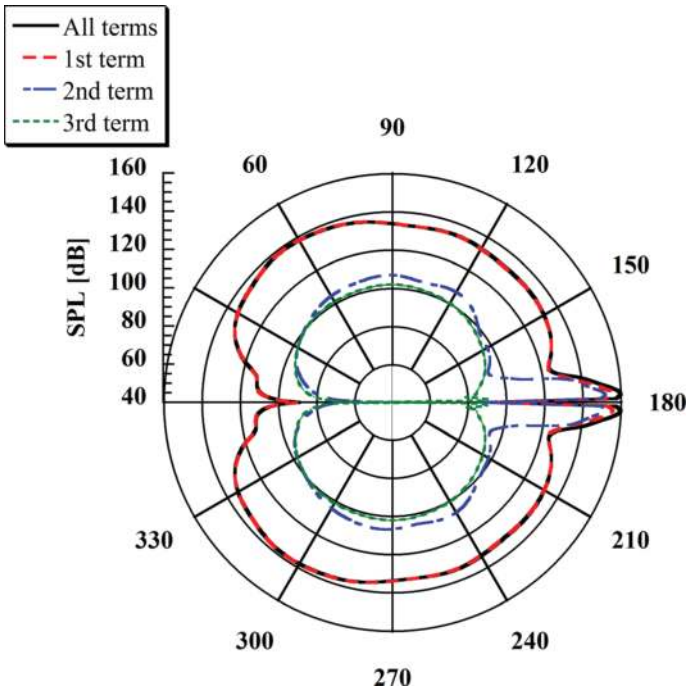

Figure 18. Polar plots of sound pressure levels predicted by decoupled simulations based on all, first, second, and third terms of Lighthill's acoustic sources at the frequency of vortex shedding at $r/D = 30.0$ [24].

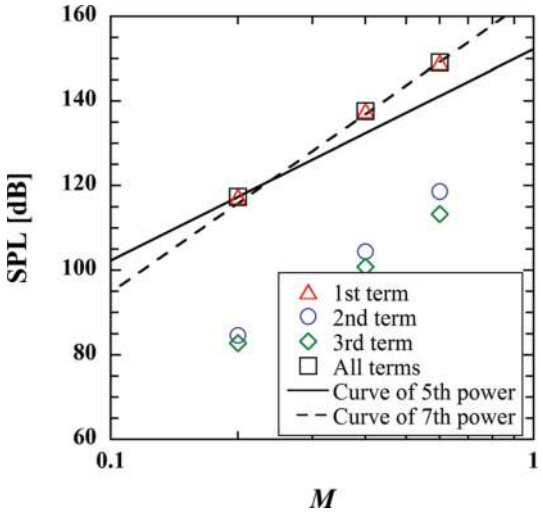

Figure 19. Effects of Mach number on sound pressure levels predicted by hybrid simulations based on all, first, second, and third terms of Lighthill's acoustic sources at the frequency of vortex shedding at $r/D = 30.0$ in the direction of acoustic propagation angle [24].

been clarified in the past research that the entropy (the second term) also needs to be taken into consideration for high-speed jets such as $M = 0.9$. Consequently, it was confirmed that only the first term needs to be taken into consideration independently of the freestream Mach number when the sound radiating from a cylinder flow is predicted on the basis of the Lighthill's acoustic analogy.

5. Conclusion

Aeroacoustic simulations composed of hybrid and direct simulations were introduced. The effects of the freestream Mach number on the flow and acoustic fields around a square cylinder were investigated. The Mach number was varied from 0.2 to 0.6. The Reynolds number based on the side length was 150. These results indicate the effectiveness and limit of the hybrid simulations.

It was found that the Strouhal number of vortex shedding, which is based on the side length, becomes lower as the freestream Mach number becomes higher. The Strouhal number for $M = 0.2$ is 0.151 and that for $M = 0.6$ is 0.144. As the Mach number increases, the velocity fluctuations of the vortices shed from the cylinder intensifies and the wake widens. The possible reason the velocity fluctuations of the vortices intensify is that the acoustic feedback exists like that in the oscillations in cavity flows. These effects can be found by the direct simulations.

The sound pressure level at the frequency of the vortex shedding in the direction of the acoustic propagation angle is proportional to M^7 for $M > 0.3$, while that is proportional to M^5

for $M \leq 0.3$. The decomposition of scattered and direct sound showed that the direct sound is too intense to neglect for $M \geq 0.4$. This indicates that the direct sound needs to be taken into consideration when predicting the flow-induced sound around the cylinder for $M \geq 0.4$. Also, the directivity of the acoustic field cannot be the above-mentioned modified Curle's equation for such a high Mach number.

Moreover, to clarify the contributions of each term of Lighthill's acoustic source to the acoustic field, acoustic simulations were performed using Lighthill's acoustic sources computed by the direct simulations. As a result, the momentum (the first term) of Lighthill's acoustic source was found to be dominant for all the Mach numbers while it has been clarified in the past research that the entropy (the second term) also needs to be taken into consideration for high-speed jets such as $M = 0.9$. Also, it was confirmed that only the first term needs to be taken into consideration independently of the freestream Mach number when the sound radiating from a cylinder flow is predicted on the basis of the Lighthill's acoustic analogy.

The present study has provided useful guidelines for predicting the aerodynamic sound on the basis of the Lighthill's acoustic analogy.

Acknowledgements

This work was supported by JSPS KAKENHI Grant Numbers JP26820044, 17 K06153 and through the application development for Post K computer (FLAGSHIP 2020) by the Ministry of Education, Culture, Sports, Science, and Technology of Japan (MEXT).

Author details

Hiroshi Yokoyama* and Akiyoshi Iida

*Address all correspondence to: h-yokoyama@me.tut.ac.jp

Department of Mechanical Engineering, Toyohashi University of Technology, Toyohashi, Aichi, Japan

References

[1] Strouhal V. On one particular way of tone generation. Annalen der Physik und Chemie (Third series). 1878;**5**:216-251

[2] Lighthill MJ. On sound generated aerodynamically Part I. General theory. Proceedings of the Royal Society of London A. 1952;**211**:564-587. DOI: 10.1098/rspa.1952.0060

[3] Curle N. The influence of solid boundaries upon aerodynamic sound. Proceedings of Royal Society of London A. 1955;**231**:505-514. DOI: 10.1098/rspa.1955.0191

[4] Gerrard JH. Measurements of the sound from circular cylinders in an air stream. Proceedings of the Physical Society London, Section B. 1955;**68**:453-461. DOI: 10.1088/0370-1301/68/7/307

[5] Phillips OM. The intensity of aeolian tones. Journal of Fluid Mechanics. 1956;**1**:607-624. DOI: 10.1017/S0022112056000408

[6] Inoue O, Hatakeyama N. Sound generation by a two-dimensional circular cylinder in a uniform flow. Journal of Fluid Mechanics. 2002;**471**:285-314. DOI: 10.1017/S0022112002002124

[7] Gloerfelt X, Perot F, Bailly C, Juve D. Flow-induced cylinder noise formulated as a diffraction problem for low Mach numbers. Journal of Sound and Vibration. 2005;**287**: 129-151. DOI: 10.1016/j.jsv.2004.10.047

[8] Liow YSK, Tan BT, Thompson MC, Hourigan K. Sound generated in laminar flow past a two-dimensional rectangular cylinder. Journal of Sound and Vibration. 2006;**295**:407-427. DOI: 10.1016/j.jsv.2006.01.014

[9] Howe MS. Theory of Vortex Sound. Cambridge: Cambridge University Press; 2003. 216 p. DOI: 10.1017/CBO9780511755491

[10] Powell A. Theory of vortex sound. Journal of the Acoustical Society of America. 1967;**36**:177-195. DOI: 10.1121/1.1918931

[11] Bodony DJ, Lele SK. Low-frequency sound sources in high-speed turbulent jets. Journal of Fluid Mechanics. 2008;**617**:231-253. DOI: 10.1017/S0022112008004096

[12] Okajima A. Strouhal numbers of rectangular cylinders. Journal of Fluid Mechanics. 1982;**123**:379-398. DOI: 10.1017/S0022112082003115

[13] Sheard GJ, Fitzgerald MJ, Ryan K. Cylinders with square cross-section: Wake instabilities with incidence angle variation. Journal of Fluid Mechanics. 2009;**630**:43-69. DOI: 10.1017/S0022112009006879

[14] Tong XH, Luo SC, Khoo BC. Transition phenomena in the wake of an inclined square cylinder. Journal of Fluids Structures. 2008;**24**:994-1005. DOI: 10.1016/j.jfluidstructs.2006.08.012

[15] Lele SK. Compact finite difference schemes with spectral-like resolution. Journal of Computational Physics. 1992;**103**:16-42. DOI: 10.1016/0021-9991(92)90324-R

[16] Gaitonde DV, Visbal MR. Pade-type higher-order boundary filters for the Navier-Stokes equations. AIAA Journal. 2000;**38**:2103-2112. DOI: 10.2514/2.872

[17] Thompson KW. Time dependent boundary conditions for hyperbolic systems. Journal of Computational Physics. 1987;**68**:1-24. DOI: 10.1016/0021-9991(90)90152-Q

[18] Poinsot TJ, Lele SK. Boundary conditions for direct simulations of compressible viscous flows. Journal of Computational Physics. 1992;**101**:104-129. DOI: 10.1016/0021-9991(92)90046-2

[19] Kim JW, Lee DJ. Generalized characteristic boundary conditions for computational aeroacoustics. AIAA Journal. 2000;**38**:2040-2049. DOI: 10.2514/2.891

[20] Colonius T, Lele SK, Moin P. Sound generation in a mixing layer. Journal of Fluid Mechanics. 1997;**330**:375-409. DOI: 10.1017/S0022112096003928

[21] Terakado D, Nonomura T, Oyama A, Fujii K. Mach number dependence on sound sources in high mach number turbulent mixing layer. Proceedings of 22nd AIAA/CEAS Aeroacoustics Conference; 30 May–1 June 2016; Lyon, France: AIAA; 2016. p. 1-10

[22] Yokoyama H, Kato C. Fluid-acoustic interactions in self-sustained oscillations in turbulent cavity flows. I. Fluid-dynamic oscillations. Physics of Fluids. 2009;**21**:105103-13-1105103-1. DOI: 10.1063/1.3253326

[23] Roshko A. On the drag and shedding frequency of two-dimensional bluff bodies. National Advisory Committee for Aeronautics Technical Note. 1954;**3169**:1-29

[24] Yokoyama H, Iida A. Identification of dominant acoustic sources in flows around square cylinder in a uniform flow. In: Computational Modeling, Simulation and Applied Mathematics. 2016; Chapter of ECTE2016:125-129